Robust Design and Evaluation of a Novel Modular Origami-Enabled Mobile Robot (OSCAR)

Oyuna Angatkina
Department of Mechanical
Science and Engineering,
University of Illinois,
Urbana-Champaign,
Urbana, IL 61801
e-mail: angatkin@illinois.edu

Andrew G. Alleyne
Fellow ASME
Department of Mechanical
Science and Engineering,
University of Illinois,
Urbana-Champaign,
Urbana, IL 61801
e-mail: alleyne@illinois.edu

Aimy Wissa[1]
Department of Mechanical and
Aerospace Engineering,
Princeton University,
Princeton, NJ 08540
e-mail: awissa@princeton.edu

*This article presents critical design modifications for an **O**rigami-enabled **S**oft **C**rawling **A**utonomous **R**obot (OSCAR). OSCAR's upgraded design mitigates motion uncertainties, which often plague soft robots. More specifically, we present a design that mitigates motion uncertainties caused by the feet interaction with the ground and uncertainties in the assembly procedures and actuators' control. The new design has a robust and repeatable locomotion cycle that reaches more than 95% of its ideal, analytically predicted locomotion cycle. OSCAR's performance is experimentally validated using two case studies, namely, navigation in a 2D environment with static obstacles and coupled locomotion of two docked OSCAR segments. Results from the first case study demonstrate OSCAR's accurate and robust path following performance across multiple trials and experiments. Results from the second case study show the successful and repeatable earthworm-inspired locomotion of two docked OSCAR segments. The second case study demonstrates OSCAR's modular design. OSCAR's modified design, along with the reduced motion uncertainty, allows for operation where individual segments can operate alone or while docked to other segments. The repeatable and modular OSCAR design presented in this study expands the operational envelope for origami-enabled robots and allows their deployment in various applications.* [DOI: 10.1115/1.4054361]

Keywords: origami robots, modular robots, bio-inspired robot design, soft robots

1 Introduction

The field of soft mobile robotics is proliferating today and has led to the emergence of various soft robot designs [1,2]. The body compliance of soft robots offers many benefits that are hard to achieve with traditional rigid robots. These benefits include safety for interaction with humans [1], adaptability to the unknown complex terrain of travel or environment [3–6], and motion in confined spaces [7,8].

This study is interested in a particular class of soft robots, namely, origami-enabled mobile robots [9–11]. Origami-enabled mobile robots are a new emerging class within a diverse umbrella of soft robotics [12]. Origami is made by folding a flat sheet into a complex 3D structure, and it has been recently used in several robotic applications, including soft grippers and mobile robots [13,14]. The compliance of origami structures allows for shape deformation, which can be used for navigation in obstacle-filled environments [9] or on unstructured terrains [15].

Origami robots are lightweight and easily scalable. They can also be fabricated using rapid prototyping facilities [16,17]. In addition, origami robots' actuation sources are more compact than pneumatically or hydraulically actuated mobile robots. Such reduction in actuation size and complexity facilitates control and power autonomy, i.e., onboard power supply and electronics [18]. For example, some of the smallest power and control-autonomous insect-inspired origami robots, such as the ones in Refs. [19] and [15], have a total weight under 10 g. These additional benefits of scalability, fast fabrication, and compact actuation make origami robots viable soft robotic solutions for many practical applications.

Some examples of origami robots particularly relevant to the current work include worm-like robots [7,16,20], a snake-like robot [21], and digestible crawling robots [22,23]. Among these robots, the earthworm-like robot [7], and snake-like robot [21] are multisegment robots with several rigidly attached segments. The sources of actuation for these robots include cable-driven systems with dc motors [7,21], servo motors [20], shape-memory alloy actuators [7,15], or external stimuli, e.g., magnetic fields [22,23]. Their potential applications are highly diverse, including noninvasive medical procedures [22,22], in-pipe inspections [7], and search-and-rescue missions [20,21].

Although compliance introduces many benefits, it also makes the soft robots underactuated [1,9,24]. As a result, many soft mobile robots have significant motion uncertainties, which presents a major challenge. Motion uncertainties hinder task-level control implementation. For example, soft mobile robots have challenges following complex paths commanded by a high-level controller. Hence, their application in real-world tasks is currently less feasible than traditional rigid mobile robots. Tailoring the physical design, sensing architecture, and subsystem integration can reduce motion uncertainties and enable robust and reliable soft robot performance [24].

This article presents the design of a novel origami-enabled soft mobile robot called OSCAR (*O*rigami-enabled *S*oft *C*rawling *A*utonomous *R*obot). OSCAR uses two origami towers to mimic a caterpillar-like crawling locomotion. Compared to other soft robots, OSCAR offers the following advantages:

- OSCAR's design relies on origami towers that are actuated using a compact, lightweight, and inexpensive servo motors. Such actuation allows for untethered operation and simplifies the control strategies.
- OSCAR's components are fabricated using rapid prototyping, allowing for multiple iterations, fast assembly, and ease of part replacement.
- OSCAR's design is modular. OSCAR can operate in single- or multiple-segment configurations, which allows for operation in the case of component or segment failure.

The design discussed in this article represents a major modification to a previous robot design that was presented in Refs. [25–27] and demonstrated basic functionality but limited locomotion.

Significant motion uncertainties limited the initial design due to unpredictable interactions between the feet and ground, including slipping, as well as considerable actuator input uncertainties. As a result, these uncertainties have prevented task-level autonomy (e.g., autonomous navigation) and system-level integration (e.g., multisegment locomotion).

This article aims to reduce motion uncertainties and highlight the effect of such improvements using two case studies. We first present three design modifications to reduce motion uncertainty. More specifically, we modified the feet design, the robot assembly procedure, and the control of the input servo motors. Then, two case studies are selected to highlight the effect of the reduced motion uncertainty. For both case studies, OSCAR performance is demonstrated both experimentally and through simulations. In the first case study, OSCAR navigates a 2D environment with static obstacles, while in the second case study, we demonstrate a coupled locomotion of two connected OSCAR segments.

The remainder of this article is organized as follows. Section 2 presents the robot design and discusses the design modifications for uncertainty mitigation. Section 3 describes the experimental setup and results used to assess the effects of the design modifications on motion uncertainties. OSCAR performance is then evaluated through the two case studies in Sec. 4. Finally, this article concludes with a summary in Sec. 5.

2 OSCAR Design

2.1 Previous Robot Design.
The preliminary design of OSCAR is shown in Fig. 1 and was described in Refs. [25–27]. The main robot components are two origami towers of opposite chirality. The towers convert rotational input into linear translation. Each tower consists of six Kresling cells and has relief cuts between every two consecutive cells to allow the robot to turn. The towers are rigidly attached to the robot's front plate and are driven by continuous rotation servo motors. The servos are rigidly mounted on the robot's back plate. When the servo rotates, the origami tower expands or contracts depending on the direction of rotation.

The robot has anisotropic friction feet at the bottom of its front and back plates to enable crawling locomotion. The feet have low friction in the forward direction and high friction in the backward direction to prevent undesirable backward slippage. The anisotropic friction feet and the origami towers' expansion and contraction result in caterpillar-like crawling locomotion.

This initial design had anisotropic friction feet based on a wedge design; each foot had low-friction material on its front side and high-friction material on its backside. During locomotion, the friction sides switched passively due to inertia and direction of motion. In addition, the robot had protective bellows (transparent

polyethylene terephthalate (PET)) whose primary function was to provide torsional rigidity. The rigidity prevented the plates from pivoting relative to the ground connection point. Finally, the preliminary robot design had open-loop controlled locomotion with an onboard microcontroller and power source.

The initial robot design demonstrated the robot's capabilities for untethered motion in a 2D planar environment, but it had several shortcomings. These shortcomings resulted in significant motion uncertainties. More specifically, the initial robot design had the following problems:

- Although the wedge feet are anisotropic, they had high backward slippage. For example, the back plate slid backward instead of being fixed during expansion, reducing the forward motion stroke. Similarly, during contraction, the front plate slid backward. This slippage reduced the efficiency of both turning and forward motion and led to significant motion uncertainties.
- The feet's interaction with the ground was irregular and hard to control. An experimental evaluation revealed that some of the feet were sometimes slightly lifted off the ground after assembly, further exacerbating the uncertainties. A similar problem occurred in the origami snake robot in Ref. [21], where weight was added to the robot's wheels to ensure even contact with the ground. However, this solution is not feasible for OSCAR due to its load-carrying limit.
- Finally, the open-loop control of the actuators' input made the actual angular position of the actuator, and hence the tower expansion/contraction, uncertain.

Therefore, the initial design's three primary sources of uncertainties are the feet design, uneven interaction between the feet and the ground, and actuator input uncertainty. To address each of these uncertainties, we have changed the initial robot design to OSCAR's current design.

2.2 Current Design.
The current design for OSCAR is presented in Fig. 2, and its characteristics are listed in Table 1. As listed, its length at the fully contracted and fully expanded states are 95 and 155 mm, respectively. Its height and width are 72 mm and 106 mm, respectively. As in the initial design, OSCAR's main elements are two opposite chirality origami towers. One end of the origami towers has a paper disk to fix the towers to the front plate rigidly through acrylic plates. The opposite end of the tower is driven by the servos and has a connector for ease of connection to the servo horn. The servo horn has a magnetic encoder ring to measure the angular position (Fig. 2(c)). Both servo horn and its connector are custom made. The encoder chip is installed on the back acrylic plate for alignment purposes.

OSCAR can move forward, turn left, and turn right. As shown in Fig. 2, OSCAR's control inputs are angular rotations of the origami towers, $[\varphi_1, \varphi_2]^T$. From the robot's fully contracted state (Fig. 3, top), positive servo angles result in the robot's expansion (Fig. 3, middle). Then, zero reference angles $[0, 0]^T$ return the robot to its fully contracted state, as shown in Fig. 3 (bottom). When equal angular expansion inputs are provided to the towers, they expand equally, and hence, the robot moves forward. When the angular inputs are different, the robot turns. Based on these considerations, OSCAR's motion is discrete and is defined as a sequence of locomotion cycles. A single expansion and contraction characterize a single cycle. The only control inputs to the robot are the tower rotational angles. In other words, the expansion of each tower is synchronized to the rotation of the servos. Also, since there are no resonances in the tower expansion, and the servos rotate at approximately a constant rate between startup and slowdown, the rates of tower expansion and contraction are constant. Thus, the tower dynamics are very simple and are subsumed by the cycle-to-cycle behavior that is the focus for the rest of this article.

Unlike previous designs, the current OSCAR design does not have protective bellows. The bellows incurred significant turning
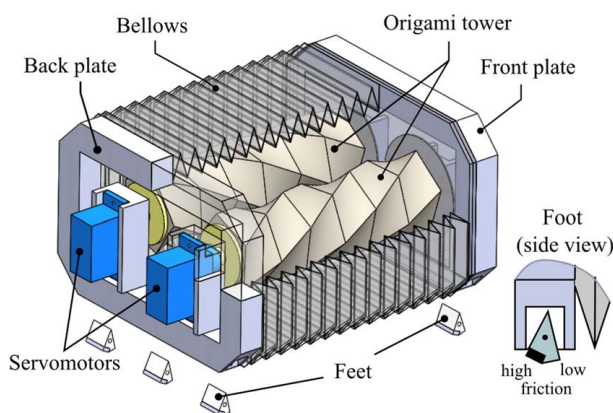

Fig. 1 The initial origami robot design. Electronics at the back plate are not shown. Image is adapted from Ref. [25].
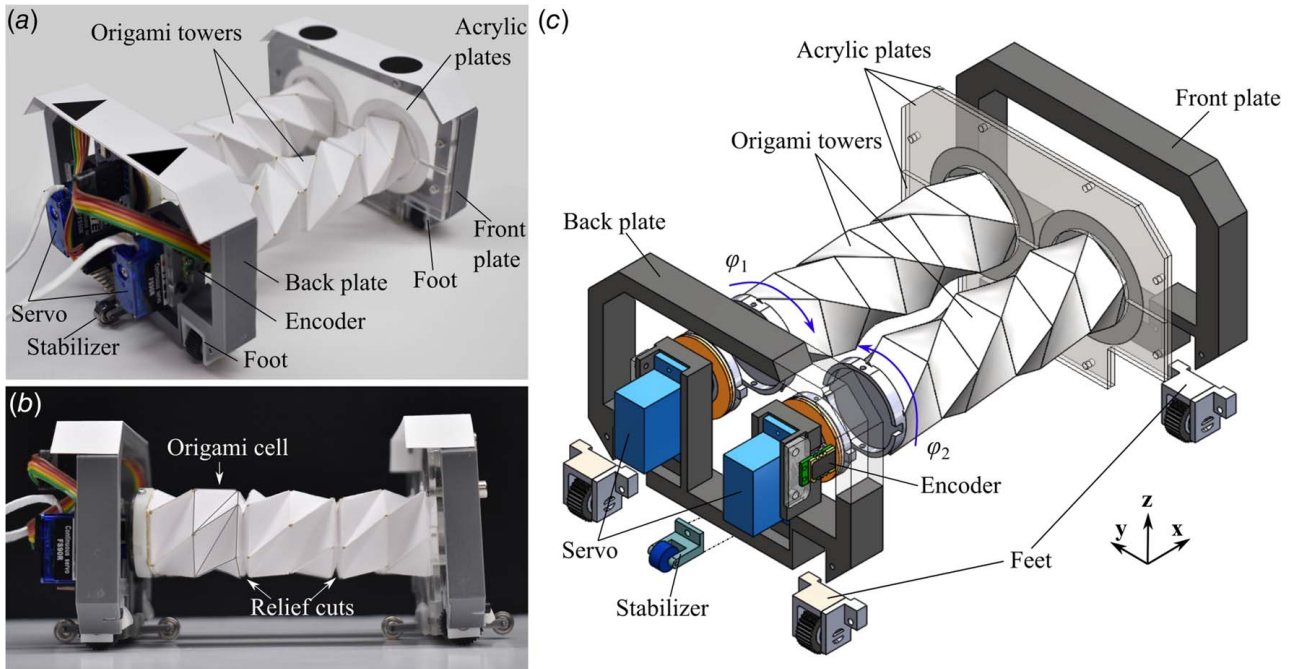
Fig. 2   The current OSCAR design showing (a) the main components, (b) a side view, and (c) an exploded CAD view

Table 1   Summary of OSCAR physical characteristics

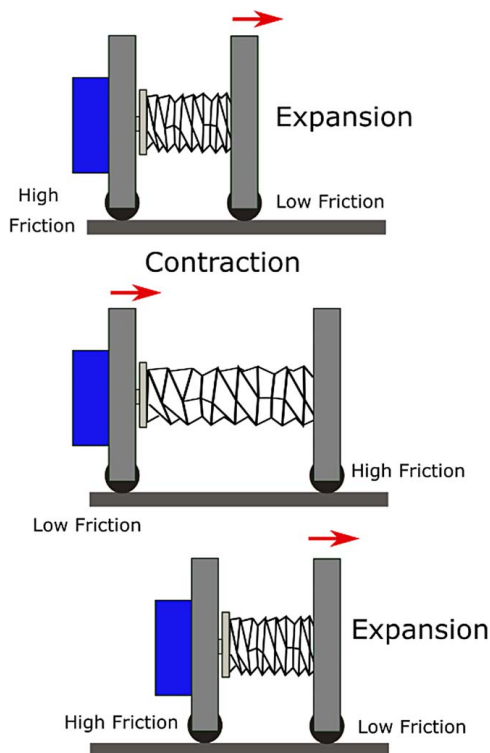| Contracted length (nominal) (mm)	Expanded length (mm)	Width (mm)	Height (mm)	Mass (g)	Number of origami towers	Speed	Number of feet
95	155	106	72	165.3	2	9.6 mm/s or 0.1 bl/s	4

Fig. 3   OSCAR locomotion cycle schematic

resistance and limited the operational range of the earlier design iterations. Thus, removing the bellows allowed a larger turn curvature (i.e., smaller turning radius) for the same angular inputs. In the most recent OSCAR design (Fig. 2), the bellows are replaced with small support wheels, called stabilizers. The stabilizers are located on each side of the front and back plates, and they prevent pivoting relative to the ground connection point. The stabilizers are located at some vertical offset from the ground.

Unlike other soft mobile robots, OSCAR's design allows for a modular robot design. It has docking and segmentation mechanisms, shown in Fig. 4, allowing it to connect to or disconnect from other OSCARs. Modularity is important for many practical applications, as it enables robust operation [28]. There are several rigid robots that feature docking and segmentation mechanisms [29]; however, these features are not as common for current soft robots. Modularity and segmentation are particularly relevant for soft mobile robots because they have a higher potential for damage in unstructured terrains due to their material compliance. Several existing origami-enable robots have multiple segments; however, these segments tend to be rigidly attached to one another making segmentation and reconfigurability in the presence of damage infeasible. For example, the soft meshworm robot in Ref. [30] has a single continuum body. The origami-based worm robot [31] and snake robot [21] have multisegmented bodies that are rigidly coupled segments. These robots could potentially fail the task execution if a part of the robot becomes trapped or faulty. Instead, OSCAR can safely disconnect faulty segments and continue its mission. OSCAR's segmentation and docking mechanisms are presented in Fig. 4. The docking is done passively using permanent magnets, and segmentation is enabled by the shape-memory alloy (SMA) actuators. The front plate for a given
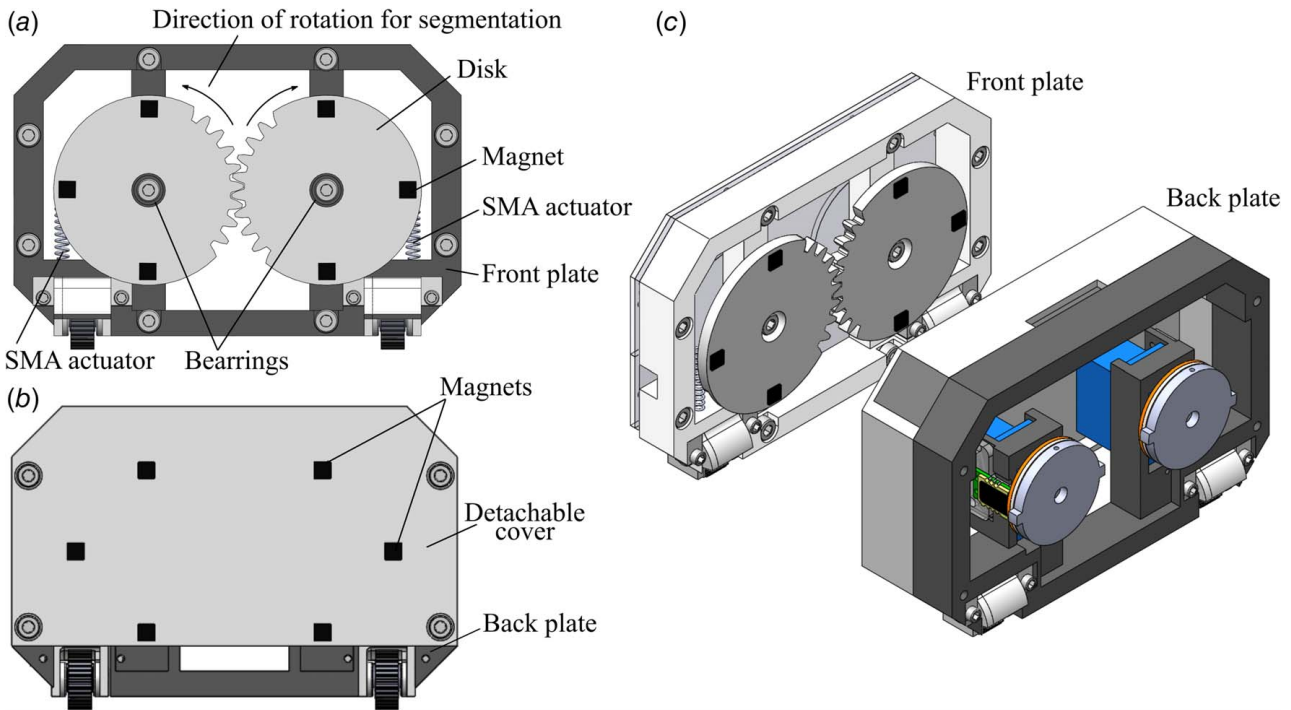
Fig. 4 Segmentation and docking mechanism: (a) front plate, and (b) back plate, (c) Isometric view of two segments during passive magnetic docking. Only adjacent front and back plates of two connecting segments are shown. During segmentation, two shape-memory alloy (SMA) actuators are actuated, which makes front plate disks rotate in the opposite directions and disconnect connected segments

OSCAR segment has two disks with eight permanent neodymium magnets, and the back plate has a detachable cover with the same number of magnets. Hence, when two OSCARs are close to each other, they can passively dock (Fig. 4(c)). When the segmentation is required, two SMAs at the front plate disks actuate (Fig. 4(a)). Upon their contraction, the disks rotate in the opposite directions, shearing the magnets and disconnecting the segments. The characteristics of SMA actuators used for segmentation is detailed in Ref. [20]. The ability to dock with multiple other OSCAR segments enhances the operational envelop and functionality of the robot.

In addition to the bellows and the segmentation mechanisms, the current OSCAR robot has three design changes to mitigate the three major sources for large motion uncertainty. We have iteratively changed the feet design to meet performance specifications. We also modified the assembly process to address the unevenness of the feet interacting with the ground. Finally, to address the actuators' uncertainties, we added and analyzed a closed-loop servo position control. These design changes resulted in the current OSCAR design.

2.2.1 Iterative Feet Design. The robot feet are a crucial element of the robot design. Ideally, starting from the fully contracted state, as the origami towers expand, the robot's front plate moves forward due to the low friction at the front feet, while the back plate stays fixed due to the high friction between the rear feet and the ground (Fig. 3). Then, during contraction, the front plate remains fixed due to increased friction being deployed at the front feet, while the back plate moves forward due to low friction being deployed at the rear feet. However, in reality, the initial foot design had high backward slippage, resulting in motion uncertainty. Multiple foot design iterations have been performed to mitigate the backward slippage and achieve better robot maneuverability.

The timeline for the designs is shown in Fig. 5. Starting from the wedge feet that resulted in high motion uncertainties, three additional designs were considered: wheels with a ratchet mechanism, a combination of wheels and wedges, and sliding ratchet feet.

The timeline highlights each design's advantages and disadvantages and shows gradual functionality improvement.

As stated earlier, the simple wedge foot design had irregular switching between its high- and low-friction phases leading to uncertainty. Thus, the wedge feet resulted in extensive backward slippage and a relatively large turning radius (i.e., poor turning capability). Wheels with ratchet mechanisms were utilized to improve the passive friction deployment of the wedge foot design and improve the robot's turning. These feet demonstrated controllable deployment and better turning capability. However, mechanical contact within the ratchet mechanism caused the supposed free-rolling, low-friction motion within each wheel to have significant friction. This friction was also subject to manufacturing variance and was not highly repeatable. The third design iteration addresses
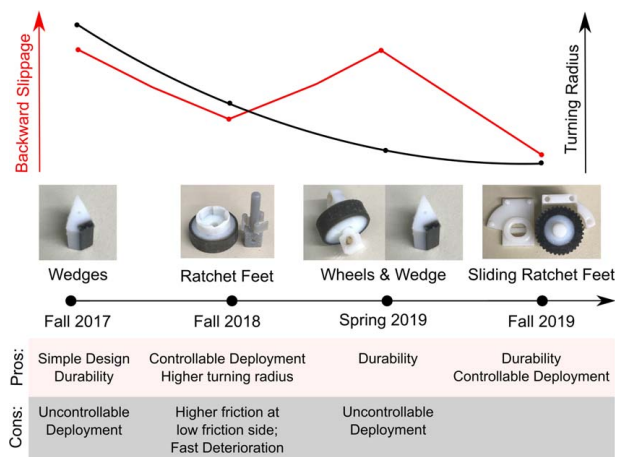

Fig. 5 Timeline of the foot design with main advantages and disadvantages of each design. The top part highlights the qualitative reduction in the backward slippage and improvements in the radius of turn (i.e., better turning)
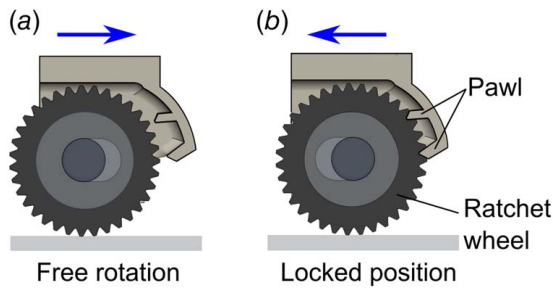
Fig. 6 Sliding ratchet feet function for (a) forward and (b) backward direction

that by combining two wheels at the sides of the plate and one wedge at the center. These feet combined the benefits of the two previous designs (see design Pros in 5). However, it also resulted in high backward slippage.

Considering the lessons learned during the evolution of the feet, we developed a design called sliding ratchet feet (Fig. 6). It utilizes wheels for turning and a low-friction ratchet mechanism for passive friction deployment. Both front and back plates have two sliding ratchet feet mounted at the bottom (Fig. 2). The foot's mechanism resembles a ratchet mechanism with the ratchet wheel freely sliding between two states: locked and free-rotation positions (Fig. 6). Switching between these states happens passively due to inertia and ground friction. When the robot plate moves forward, the ratchet wheel slides back to a position where it can freely rotate, providing low friction for the plate's forward motion (Fig. 6(a)), and when the plate is driven backward, the ratchet wheel encounters two pawls and stops. The feet provide high friction in this locked position and prevent undesirable plate backward slippage (Fig. 6(b)). This design offers robust feet performance with low backward slippage, thereby enabling a low turning radius for the robot (Fig. 5).

2.2.2 OSCAR Assembly Process. The next design improvement ensures even ground contact among all the feet and ground. A repeatable assembly procedure for OSCAR is important for creating an even interaction between all the robot's feet and the ground. The assembly process from the previous system design was modified, as shown in Fig. 7. During the assembly, both the front and back plates are rigidly fixed to the custom-designed assembly

guide (Fig. 7). The assembly guide aligns the bottom of both the front and back plates (in the x–y plane), thus guaranteeing uniform foot-ground interaction for all feet.

The assembly process is summarized in the block diagram in Fig. 8. The front and back plates are pre-assembled first, such that the back plate has installed origami towers that are left disconnected from the front plate. The plates are then fixed at the assembly guide that aligns them vertically and horizontally and maintains the plates' distance to $dl = 41$ mm (Fig. 7).

A LABVIEW VI and the microcontroller start and initialize the robot servos. During the initial power on, the continuous rotation servos could change their position—this is a common phenomenon for small-scale servos. Thus, aligning servo positions after their initialization and then fixing the origami towers at the front plate prevents any prestress in the towers after assembly and allows even foot and ground interaction (Fig. 7(b)). Finally, the assembled robot is released from the guide.

The robot re-assembly (Fig. 8) is repeated at the beginning of each experiment for performance consistency. At re-assembly, the origami towers are released from the back plate and then fixed to the front plate in the assembly guide to eliminate the uncertainties, as described in Fig. 8.

2.2.3 OSCAR Actuator Control. The actuators' input uncertainty is one of the major contributors to OSCAR's motion uncertainties. In this design modification, we added a servo position controller, where the servo angular positions are controlled by simple proportional-integral (PI) controllers, which are generally sufficient for servo motor position control. The controller input u is the servo's pulse-width modulation (PWM) input. The same controllers are used for both left and right servos and were implemented on OSCAR's microcontroller. The angular positions are regulated to be within ± 2 deg of the reference value to avoid any origami tower damage.

The controller has a standard form of

$$\Delta u = K_p e + K_i \int_0^t e(t)\, dt \qquad (1)$$

where $e = \varphi_{ref} - \varphi$ is the error between the reference and measured servo angles, and K_p and K_i are proportional and integral gains, respectively. This control input is bounded $\underline{\Delta u} \leq \Delta u \leq \Delta \overline{u}$ and subjected to the integral anti-wind-up constraint $\left| K_i \int_0^t e(\tau)\, d\tau \right| \leq \alpha$.
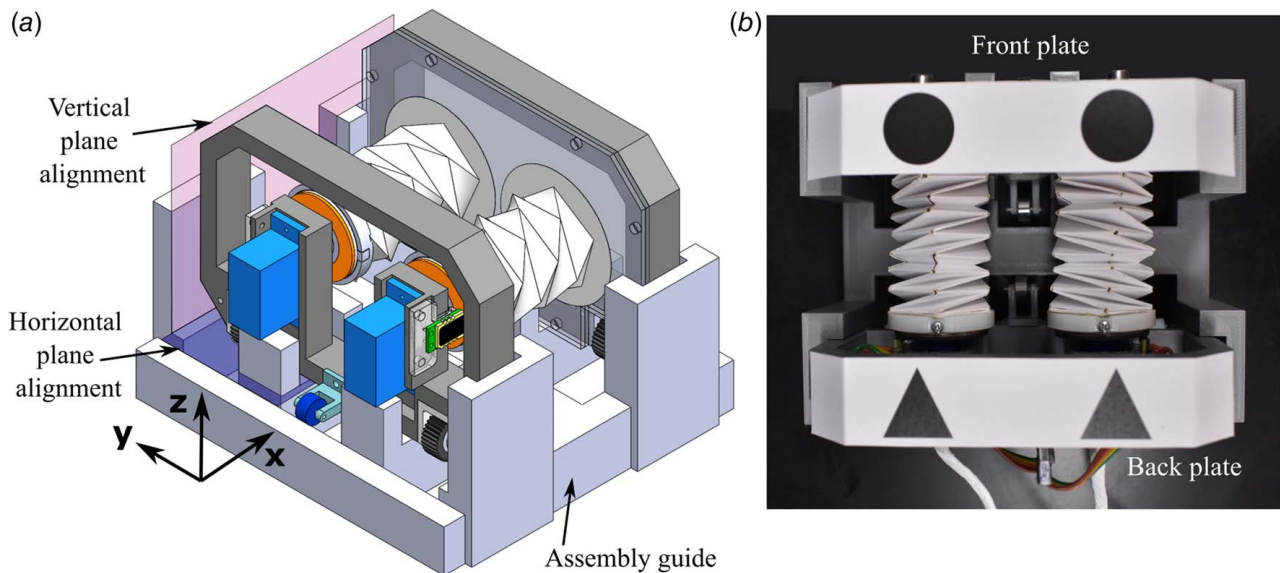

Fig. 7 Robot during assembly in the assembly guide: (a) isometric CAD view and (b) top view of the actual robot. The guide allows to align front and back plate in vertical (x–z) and horizontal (x–y) planes preventing uncertainties due to feet with ground interaction
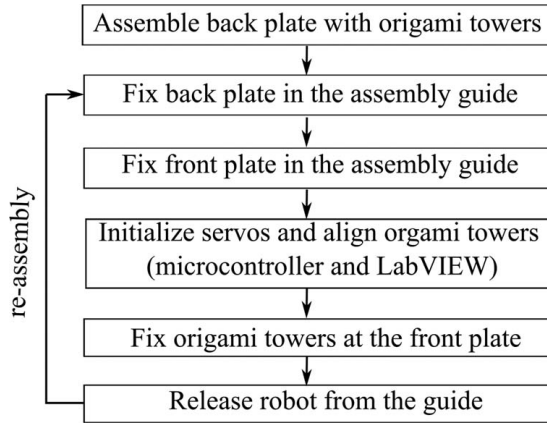
Fig. 8 Robot assembly process with the guide

Fig. 9 Experimental testbed

The servo has a deadband near-zero control inputs. This deadband is detrimental to accurate servo motion. To compensate for this, the deadband was manually aligned to be symmetric in the $[-\delta, \ \delta]$ range with respect to $\Delta u = 0$ and compensated, resulting in the final PWM input having a form of

$$u = 90(1 + s\Delta u + d) \tag{2}$$

$$d = \begin{cases} \delta, & \text{if } \Delta u > 0 \\ -\delta, & \text{if } \Delta u < 0 \end{cases} \tag{3}$$

Here, d is the added deadband compensation and the constant $s = \pm 1$ corresponds to the origami tower chirality, i.e., positive or negative. The PWM input is given by the Arduino command, where 90 corresponds to zero servo speed. Hence, the multiplier 90 is added. The uncertainty mitigation with this low-level servo position control is validated in Sec. 3.

3 Motion Uncertainty Assessment

3.1 Experimental Setup. To assess the effects of the previously mentioned design changes, we built an experimental setup where the position and orientation of an OSCAR segment could be measured. The experiments are performed in the testbed, as shown in Fig. 9. It has a camera (USB-72, Leopard Imaging) mounted on top of the frame, having a "god's eye" view of the workspace, and an offboard personal computer (PC). The PC is used for robot localization and for computing the angular inputs in LABVIEW VI. Since this work focuses on uncertainty mitigation, OSCAR has an offboard Arduino microcontroller and 5V power source for powering servos. These elements could be miniaturized and placed onboard, but that is outside the current work scope.

Localization is done using four black-and-white markers on OSCAR (Fig. 9). There are two markers per plate, which provide the plate's position $[x, y]$ and orientation θ. When the camera takes an image, the markers are localized via image processing using geometric matching. The robot state, which is $[x, y, \theta]^T$ of the front plate, is defined with respect to the local coordinate frame fixed at the centroid of the front plate.

When the robot arrives at the fully contracted state, the camera captures the workspace image and sends it to the PC. The LABVIEW VI localizes the robot state and defines reference angles for the current locomotion cycle, $[\varphi_1, \varphi_2]_k^T$. Here, k denotes the index of the locomotion cycle. φ_1 and φ_2 are defined by either a manual user input or a path following controller. The angles are sent to the microcontroller, where the low-level servo control achieves the desired angles, and the robot expands. Then, localization is repeated. Zero angular inputs $[0, 0]^T$ are sent for
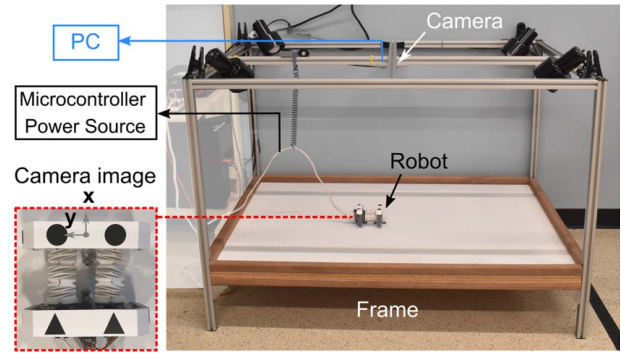
contraction. After contraction, the process repeats for the next locomotion cycle.

3.2 Results for Motion Uncertainty Assessment. The motion uncertainty of OSCAR was assessed both in forward motion and during a constant radius turn using the experimental setup detailed in Sec. 3.1. The markers on the front and back plates were localized using the overhead cameras and reference angles were input using OSCAR's actuator control algorithm.

3.2.1 Forward Motion. The effect of the motion uncertainty mitigation on the forward motion has been assessed from the robot displacement data collected for angular inputs $\varphi_1 = \varphi_2$, shown in Table 2. The displacement data are averaged over 12 locomotion cycles. As presented in Table 2, after the feet re-design alone, the displacement becomes 89% of the ideal displacement predicted by a kinematic model.[2] However, due to the remaining uncertainties, the standard deviation for the x and y displacements is significant, and the mean value for the y displacement is nonzero.

The average displacement per locomotion cycle becomes more consistent after implementing the new assembly process and adding the deadband compensation in the low-level controller. Finally, after changing the low-level controller's input from step references to ramp references, the error between the measured and model-predicted displacement falls below 4.2%, and the mean y displacement approaches zero. While changing the low-level controller's reference to a ramp seems to have an insignificant effect during forward motion, this change affects turning significantly.

3.2.2 Turning. The motion uncertainties during turning have been assessed by evaluating the OSCAR displacement data for the range of the static angular inputs within its achievable workspace.[2] The reference angles are defined through their angular ratio, such that $\varphi_2/\varphi_1 \in [1/\bar{r}, \bar{r}]$, where $\bar{r} = 1.6$ based on the robot's construction. The maximum angular input to the origami tower is $\varphi_{\max} = 180$ deg. Here, ratios $1/\bar{r}$ and $\bar{r}$ correspond to the maximum right and left turns, respectively. Reference angle ratios close to 1, 1/2, and 1/4 of $\bar{r}$ are used in Fig. 10.

For the best robot performance, the towers should expand uniformly during locomotion and symmetrically during turning. Even after the assembly procedure revisions and feet design improvements, initial experiments revealed large asymmetry between the left and right turns. Two modifications were made to the hardware and low-level position controllers to achieve uniform and symmetric expansion.

OSCAR's origami towers are of opposite chirality, and thus, the servos need to rotate in the opposite direction during the robot expansion. However, as stated earlier, the servos have deadbands. If the two servo deadbands are misaligned, the towers expand non-

---

[2]https://youtu.be/OWI3YgtUdmk

Table 2 Forward displacement assessment

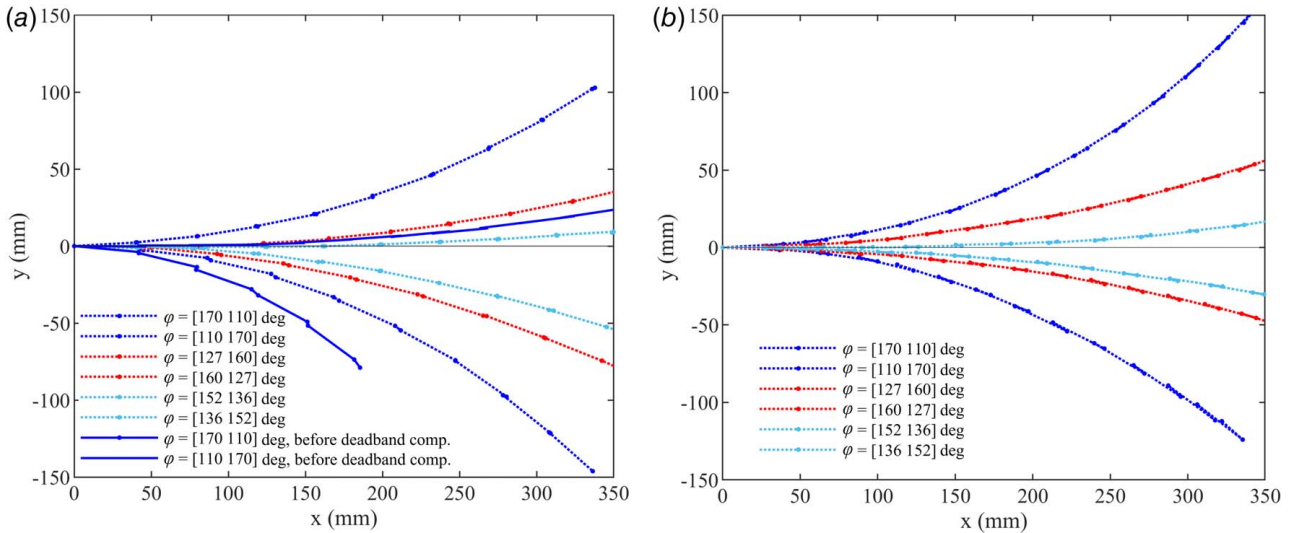| Design iteration	$[\varphi_1\ \varphi_2]^T$ (deg)	x_{mean} (mm)	Std. dev. (mm)	y_{mean} (mm)	Std. dev. (mm)	$x_{mean}/x_{kin.mod.}$ (%)
After feet re-design	[150 150]	28	7.8	−4	1.75	89
After feet re-design, assembly change, and deadband compensation at the low-level control	[144 144]	27.7	1.74	−1.3	0.74	93
After feet re-design, assembly change, deadband compensation, and ramp input at the low-level control	[144 144]	28.5	1.79	−1	0.51	95.8

Fig. 10 Robot displacement for the range of static inputs (in deg): (*a*) step angular input and (*b*) ramp angular input

uniformly. This misalignment results in a significantly biased turning displacement, where the robot "pulls" to one side of the centerline (solid lines in Fig. 10(*a*)). The displacement becomes more symmetric with respect to the horizontal axis when the deadbands are manually aligned to be symmetric in the left and right directions. The deadbands are compensated with the approach given in Eqs. (2) and (3), which results in more symmetric turning, as indicated by the dotted lines in Fig. 10(*a*).

Smoother and more constant expansion speed in the robot can be further achieved by providing a ramp reference angle instead of a step command to the low-level servo position controller. The best ramp slope (i.e., desired tower expansion/contraction speed) was empirically determined to be 5.9 rad/s for OSCAR's current design but could change with different robot designs. Figures 10(*a*) and 10(*b*) show the data comparison for the step and ramp
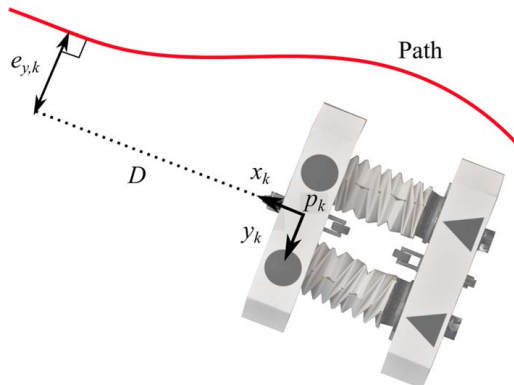

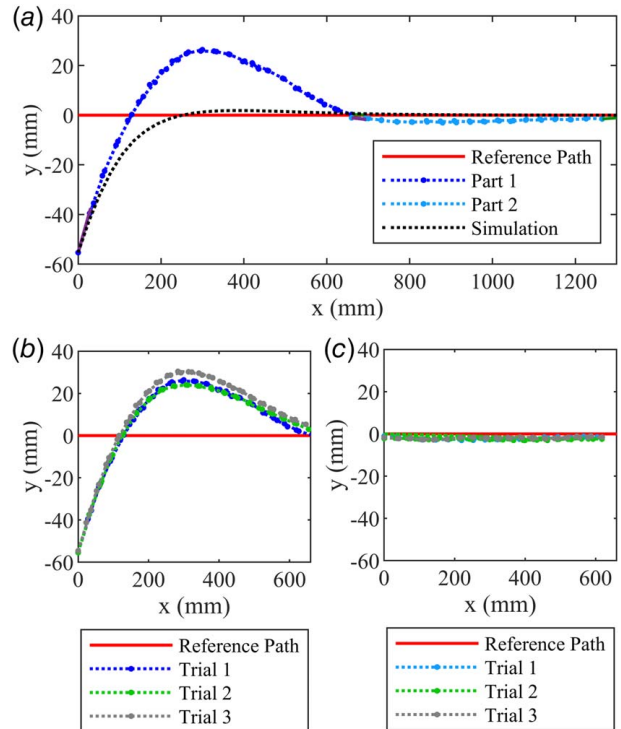Fig. 11 Lateral error in the feedback control

Fig. 12 Straight-line following with initial offset: (*a*) combined experimental results. The final robot orientation and *y*-coordinate in experiment 1 matches the same in the initial state for experiment 2, (*b*) and (*c*) Trajectory repeatability for three trials in settings of experiment 1 and experiment 2, respectively

reference inputs in the low-level servo position controllers, respectively. With step references, the servo inputs saturate due to large errors. Since the two tower-actuating servos rotate in opposite directions, even small misalignments of the servo deadbands cause differences in servo speeds at saturation, which results in a significant displacement bias. On the other hand, with ramped angular references, this is not an issue as the robot's servos track both position and speed. Manually compensating the deadband and using a ramp reference input result in a more symmetric robot displacement (Fig. 10(*b*)), demonstrating the mitigated motion uncertainties.

4 Case Studies

This section demonstrates OSCAR performance by investigating two case studies: autonomous navigation in a 2D environment with static obstacles and coupled locomotion of two OSCAR segments.

4.1 Case Study I—Navigation in the Presence of Obstacles

4.1.1 Methods. This case study investigates OSCAR's navigation in a 2D environment with and without obstacles. The navigation consists of path planning using the well-known hybrid A* algorithm and path following using a proportional feedback controller. As stated earlier, OSCAR motion is discrete or defined in terms of locomotion cycles.

(a) Path planner

As shown in Fig. 10(*b*), OSCAR's lateral and forward motions are coupled by a nonholonomic constraint, and it has a limited range of motions defined by $\varphi_2/\varphi_1 \in [1/\bar{r}, \bar{r}]$. Hybrid A* accommodates these constraints. It is a graph search method designed for rigid-body robots with nonholonomic constraints, e.g., cars [32]. The planner plans a path by growing a search tree through the recursive application of a finite set of motion primitives until reaching the desired goal state. The set of motion primitives is constructed by discretization of the robot's achievable workspace. As a result, it outputs a feasible path from the given start state to the desired goal state. Details about Hybrid A* path planning are given in Refs. [32–34]. Variation of this planner, called a bidirectional A*, was previously applied to a soft snake robot in Ref. [35].

The reference path is planned using MATLAB's Navigation Toolbox with constraints on robot turning radius $|R| \leq R_{max}$, where $R_{max} = 467.6$ mm, and total forward displacement, $ds = 30$ mm for a single locomotion cycle. Here, $|R| \leq R_{max}$ is the same as $\varphi_2/\varphi_1 \in [1/\bar{r}, \bar{r}]$. During planning, the robot is considered as a point. Thus, an additional clearance space around obstacles of size $df = 65$ mm, accounting for its lateral dimensions, is used for obstacle avoidance. A band with a radius of the clearance size is added to the actual obstacle during planning.

(b) Path following controller

The path following control has control inputs in the longitudinal and lateral directions that are coupled to determine the robot's angular inputs. The path following controller was first presented in Ref. [25]. The x-axis of the local coordinate frame, shown in Fig. 11, corresponds to the longitudinal direction, and the y-axis corresponds to the lateral direction. This controller is similar to the path following control problem in rigid-bodied robots [36], such as cars. They have a longitudinal controller to regulate forward speed and a lateral controller to minimize the normal error to the path and control the steering angle.

Assuming OSCAR moves with a constant speed, its longitudinal control input is constant and can be expressed as follows:

$$u_{x,k} = \rho u_{x,max} \qquad (4)$$

where $\rho = 0.8$, and $u_{x,max}$ is the maximum longitudinal control input, which corresponds to the origami tower's maximum angular input ($u_{x,max} = \varphi_{max} = 180$deg). The subscript k denotes the index of the current locomotion cycle.

The lateral control input is a simple proportional controller for this proof of concept:

$$u_{y,k} = K_p e_{y,k} \qquad (5)$$

where K_p is a proportional gain and $e_{y,k}$ is the lateral error normal to the path, as shown in Fig. 11. The error $e_{y,k}$ is defined between the reference path and the point in a preview distance, D, from the current position, p_k. The preview distance, D, is a user-defined parameter tuned for the controller stability. For this case study, the feedback controller gains were determined empirically to be $K_p = 0.7$ and $D = 250$ mm.

The longitudinal and lateral control inputs are coupled with the angular inputs $[\varphi_1, \varphi_2]^T$ as follows:

$$\begin{aligned}(\varphi_1 + \varphi_2)_k/2 &= u_{x,k} \\ (\varphi_1 - \varphi_2)_k/2 &= u_{y,k}\end{aligned} \qquad (6)$$

The average of the angular inputs corresponds to forward motion and is denoted by the longitudinal control input $u_{x,k}$, and their averaged difference corresponds to the robot's turning and is denoted by the lateral control input $u_{y,k}$. Then, $[\varphi_1, \varphi_2]^T$ from (6) can be expressed in terms of the control inputs as follows:

$$\begin{bmatrix}\varphi_1 \\ \varphi_2\end{bmatrix}_k = \begin{bmatrix}1 & -1 \\ 1 & 1\end{bmatrix}\begin{bmatrix}u_x \\ u_y\end{bmatrix}_k \qquad (7)$$

The angular inputs are subjected to the following total angular input and turning ratio constraints

$$0 \leq \varphi_i \leq \varphi_{max}, \quad i = 1, 2 \qquad (8)$$

$$\frac{1}{\bar{r}} \leq \frac{\varphi_2}{\varphi_1} \leq \bar{r} \qquad (9)$$

By using (7), the constraint (9) can be expressed as the lateral control input bound

$$|u_{y,k}| \leq u_{x,k}\frac{\bar{r} - 1}{\bar{r} + 1} \qquad (10)$$

4.1.2 Results. In this case study, the simulation results are obtained using the robot's kinematic model, previously presented as a segmented kinematic model in Ref. [25] and validated for OSCAR in the Appendix. The experimental results are obtained using the setup detailed in Sec. 3.

(a) Straight-line path following with an initial offset: This case study starts by setting the reference path to a straight line, and the robot is at an initial offset. This study demonstrates OSCAR's ability to converge to a path despite an initial offset using the simple proportional feedback controller from Sec. 4.1.1.

The reference path is a horizontal line at $y = 0$ mm, and the initial OSCAR state is $p_0 = \begin{bmatrix}x, & y, & \theta\end{bmatrix}^T = \begin{bmatrix}0, & -60, & \pi/6\end{bmatrix}^T$. Figure 12 presents the experimental and simulation results for the straight-line path following. The experimental response is a combination of two experiments. Due to the limited testbed workspace (Fig. 9), two experiments were performed sequentially, each spanning an x-displacement of 600 mm, which is the workspace limit. The final state of the first experiment, i.e., y-coordinate and orientation, is used as an initial state for the second experiment to achieve the overall response shown in Fig. 12(*a*).[3]

As shown in Fig. 12(*a*), OSCAR successfully converges to and follows the path. Its trajectory in the experiment has a slightly larger overshoot than in the simulation, but the lateral steady-state error in the y-direction stays within the measurement error of the predicted trajectory. The differences in experiment and simulation can be attributed to the simplicity of the kinematic model, which does not account for losses due to friction or additional model error.
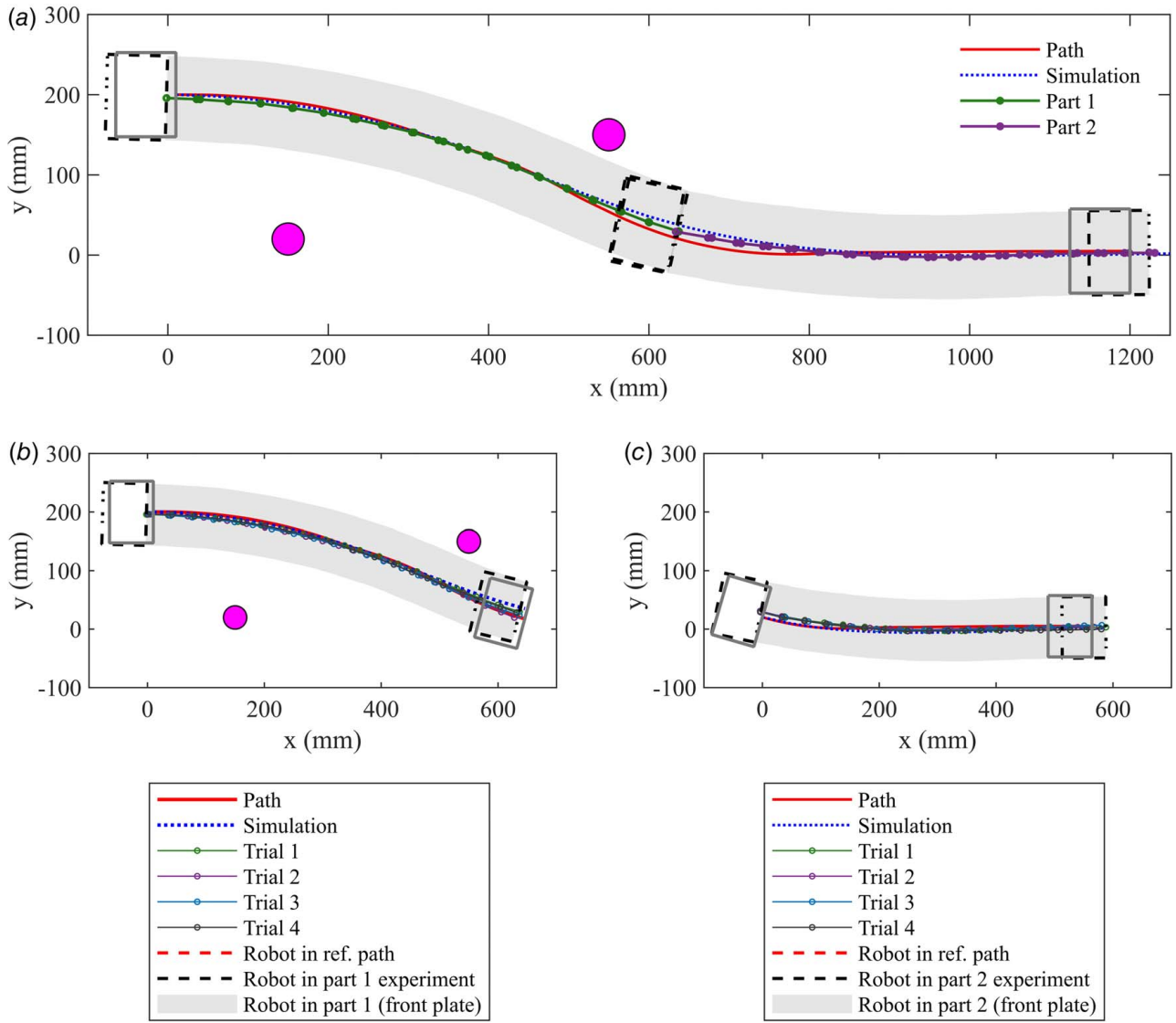
---

[3]See Note 2.

Fig. 13 2D navigation in the presence of static obstacles showing: (a) the planned path and combined experimental results. Solid and dashed-line boxes indicate the robot orientation in the reference path and the experiment, respectively. Shaded areas correspond to the robot body motion, (b) and (c) the trajectory repeatability for four trials in settings of part 1 and part 2 experiments, respectively

Part 1 and 2 experiments have been conducted three times to verify the repeatability of the results (Figs. 12(b) and 12(c)). The experimental results are repeatable due to the minimization of OSCAR's motion uncertainties.

(b) Navigation in the presence of static obstacles: This portion of the first case study demonstrates OSCAR's ability to navigate in the presence of static obstacles. OSCAR's initial and goal states are $p_0 = \begin{bmatrix} 10, & 200, & 0 \end{bmatrix}^T$ and $p_g = \begin{bmatrix} 1200, & 5, & 0 \end{bmatrix}^T$, respectively. The static obstacles have a circular shape with their radius and position specified in Table 3.

The planned path and combined navigation results are shown in Fig. 13(a). The reference path (solid line) has an s-shape with the robot having 0 rad orientation at its initial and goal states (solid line boxes). The obstacles are displayed as solid-color circles. Again, two consecutive experiments have been conducted for the complete robot trajectory to overcome the testbed size constraints. The robot initial and final states in part 1 and part 2 experiments are shown as dashed line boxes. It can be noted that the robot's actual orientation matches the desired orientation in the
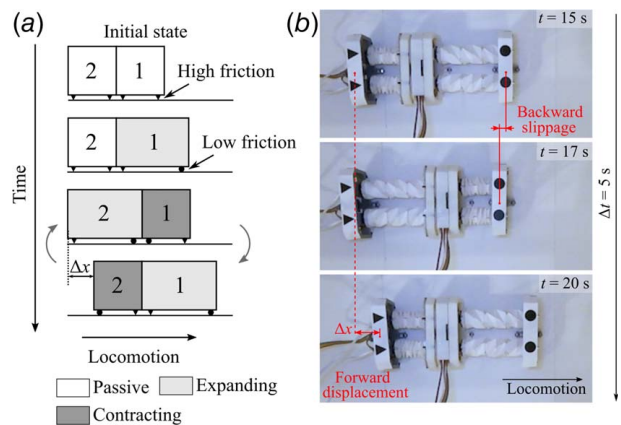

Fig. 14 Coupled locomotion: (a) gait description starting from initial state and (b) video frames depicting alternating states during locomotion

Table 3 Obstacle location and radius

Obstacle	x (mm)	y (mm)	R (mm)
Obstacle 1	150	70	20
Obstacle 2	550	150	20

reference path (dashed line boxes). The shaded area shows the robot motion, represented as the motion of the front plate.

Figure 13 shows that OSCAR successfully navigates the environment avoiding both obstacles. Moreover, the experimental path agrees with the reference path and aligns well with the simulation. Parts 1 and 2 of the experiments were conducted four times to confirm OSCAR's repeatable performance and confirm the efficacy of the design modification in reducing the motion uncertainties (Figs. 13(b) and 13(c)). The variation between the experimental trials is minimal and shows the repeatability of OSCAR's performance and ability in navigating a path repeatably and in the presence of obstacles.

4.2 Case Study II—Coupled Locomotion of Two OSCARs. The second case study investigates the coupled locomotion of two OSCAR segments to evaluate the feasibility of assembling multiple segments into a modular robot.[4] The coupled locomotion is tested during straight-line motion, where the angular inputs for each locomotion cycle are expressed as: $\left[\varphi_1, \varphi_2 \right]^T = \left[170 \deg, 170 \deg \right]^T$. The locomotion gait is shown in Fig. 14(a). Starting from two segments being fully contracted, segment one expands. Following that, segment one contracts, while segment two expands. Then the states alternate with segment one expanding, while segment two contracting. The last two steps are repeated during the robot locomotion. Figure 14(b) shows the video frames of the top view of two coupled OSCAR segments during locomotion, starting from the expansion of segment one and the contraction of segment two. Segment one contraction and segment two expansion, or vice versa, occur simultaneously to account for the anisotropic foot friction of the two connected middle plates.

The displacement time history starting from $t = 5$ s is presented in Fig. 15. The data in the time history plot correspond to the centroids of the front plate of segment one and the back plate of segments one and two. The shaded areas correspond to actuation periods during each locomotion state: I—the expansion of segment one and contraction of segment two, and II—the contraction of segment one and the expansion of segment two. The flat areas in the plot correspond to wait times for the next actuation input, which is introduced for stability. During state I actuation, both front and back plates of segments one and two move forward, while the connected middle plates stay still. More specifically, during segment one expansion, its front plate moves forward due to low feet friction, and its back plate remains fixed due to high feet friction (see Fig. 3). Similarly, during state II actuation, the contraction of segment one, its front plate feet stay still due to high feet friction, and its back plate moves forward due to low feet friction. Hence, during state I, the robot's middle-connected plates stay still, while front plates of segment one and back plate of segment two move forward. Then, during state II, the connected plates in the middle move forward, caused by both contraction of segment one and the expansion of segment two. This gait is similar to the multisegment earthworm robot gait described in Refs. [7,37].

The locomotion cycles in Figs. 14(b) and 15 show repeatable locomotion cycles for both OSCAR segments and confirm the efficacy of the docking mechanism, feet design, and low-level servo input controller.
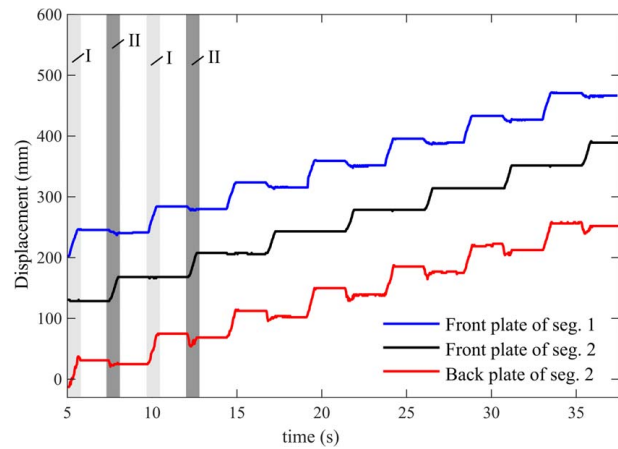
----

[4]See Note 2.

Fig. 15 Displacement time history. Shaded areas show two states: (1) state I (light gray)—segment one expansion and segment two contraction, and (2) state II (dark gray)—segment one contraction and segment two expansion. States I and II repeat recursively during locomotion, as shown for the first two locomotion cycles

5 Conclusion

This study presents a comprehensive study on the design and experimental evaluation of a novel origami-enabled modular crawling robot, OSCAR. OSCAR's current design focuses on mitigating motion uncertainties, which is a significant challenge for soft robots interacting with the terrain. For OSCAR, the uncertainties are attributed to the three primary sources, namely, the feet design, their interaction with the ground, and actuator uncertainties. As a result, the feet are extensively re-designed, the assembly process was made more repeatable through a fabrication fixture system, and the feedback servo position control was implemented and greatly improved to reduce actuator uncertainty. These design modifications reduced motion uncertainties significantly such that the current OSCAR design has a robust and repeatable performance that can achieve up to 96% of its ideal, analytically predicted locomotion cycle.

OSCAR's performance is validated using two case studies: navigation in the 2D environment with static obstacles and coupled two-segment locomotion. The first case study highlights the effects of mitigated uncertainties. As shown, using a simple proportional feedback path following controller, OSCAR can accurately navigate an environment and avoid obstacles. Moreover, it can successfully converge to the desired path when started at an offset. In addition, all the results have high repeatability, as demonstrated by several experimental trials. In the second case study, two coupled OSCAR segments can navigate in a straight line using simple actuation inputs. Alternation of the simultaneous expansion of one segment and contraction of the other segment enables locomotion. The second case study validates the feasibility of connecting multiple OSCAR segments to enable a modular robot design. Unlike existing soft robots, OSCAR can disconnect the segments when needed. The repeatable and modular OSCAR design and performance presented in this study expand the operational envelope for origami-enabled robots and allow for their deployment in various applications.

Acknowledgment

Conflict of Interest

There are no conflicts of interest.

Data Availability Statement

The datasets generated and supporting the findings of this article are obtainable from the corresponding author upon reasonable request. The data and information that support the findings of this article are freely available at: bamlab.mechse.illinois.edu The authors attest that all data for this study are included in the paper. Data provided by a third party listed in Acknowledgment.

Nomenclature

k = subscript denoting the locomotion cycle index
D = preview distance, mm
R = robot turning radius, mm
$\bar{r}$ = maximum angular input ratio, φ_2/φ_1
e_y = lateral error, mm
p_k = robot state defined at its front plate, $p = \begin{bmatrix} x, y, \theta \end{bmatrix}^T$
u_x = longitudinal control input
u_y = lateral control input
K_p = proportional gain
K_i = integral gain
φ_1 = angular input to the left origami tower, deg or rad
φ_2 = angular input to the left origami tower, deg or rad

Appendix: Kinematic Model Validation

Kinematic Model. The kinematic model, schematically presented in Fig. 16, describes OSCAR's motion for a single locomotion cycle k. It was previously presented in Refs. [25,38] (see a segmented kinematic model) and [27]. Its equations are Eqs. (7)–(15) as presented in Ref. [25].

As shown in Fig. 16, the model finds the robot state $p_{k+1} = \begin{bmatrix} x, y, \theta \end{bmatrix}^T_{k+1}$ for given angular inputs $\begin{bmatrix} \varphi_1, \varphi_2 \end{bmatrix}^T_k$ to the origami towers by solving a vector loop. The current state p_k is known. This vector loop considers origami cells' expansions, where vectors $\mathbf{R}_1, \ldots, \mathbf{R}_6$ correspond to two consecutive origami cells. Their lengths vary as functions of angular input to the corresponding tower, $f(\varphi_i)$, $i = 1, 2$. Vectors $\mathbf{R}_7$ and $\mathbf{R}_8$ at the front and back plates have equal length, which corresponds to the fixed distance between the towers.

The model has two assumptions: ideal foot friction and equal angular distribution between cells within a single origami tower. The robot's motion is represented in Fig. 16. Due to no friction losses, the robot's front plate at its expanded state corresponds to the p_{k+1} state after the locomotion cycle. Because angular input to the tower is evenly distributed among its cells, the vectors within a single tower, i.e., $\mathbf{R}_1, \ldots, \mathbf{R}_3$ or $\mathbf{R}_4, \ldots, \mathbf{R}_6$ are of equal length.
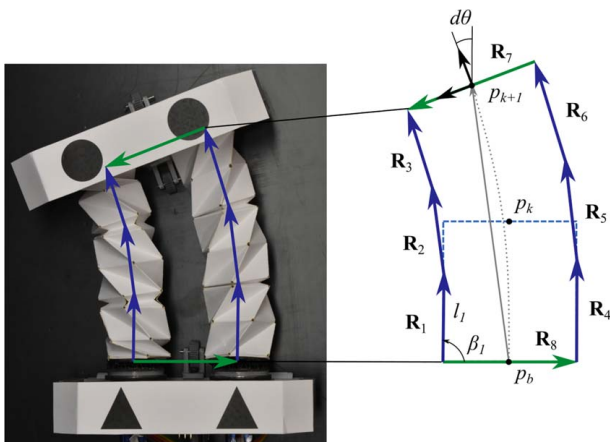

Fig. 16 OSCAR kinematic model schematic. It represents a vector loop defined by the origami towers at the expanded state.
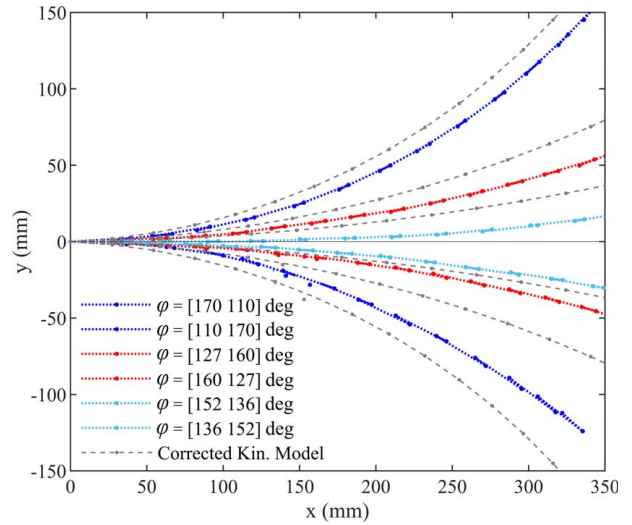

Fig. 17 Comparison of the validated kinematic model (gray dashed lines) and the experimental data for the same angular inputs

Moreover, angles between two vectors within the same tower are equal.

Validation. The model is validated by comparing the model predictions and experimental data in Fig. 10(b). The validation accounts for the friction losses in the actual feet during locomotion, which is unavoidable even with the optimized foot design. It affects the robot's orientation increment, which is smaller than predicted.

During validation, for the same angular inputs $\begin{bmatrix} \varphi_1, \varphi_2 \end{bmatrix}^T$ as in the experiments, the model outputs $\begin{bmatrix} dx, dy, d\theta \end{bmatrix}^T = p_{k+1} - p_k$ were compared with experimental data. For clarity, it should be noted that each experimental trajectory in Fig. 10(b) covers at least ten locomotion cycles. Based on the comparison, the following correction was introduced to the model outputs

$$d\tilde{\theta} = \gamma \, d\theta \qquad (A1)$$

$$\begin{aligned} d\tilde{x} &= \sqrt{(dx + d\tilde{l})^2 + dy^2} \cos\frac{d\tilde{\theta}}{2} - dl \\ d\tilde{y} &= \sqrt{(dx + d\tilde{l})^2 + dy^2} \sin\frac{d\tilde{\theta}}{2} \end{aligned} \qquad (A2)$$

where γ is empirical efficiency factor for the orientation increment, $\gamma = 0.15$. Here, dl is the length of the origami towers at the robot's fully contracted state. From the assembly guide, $dl = 41$ mm is applied in all kinematic model equations.

In this correction, Eq. (A1) corrects the orientation increment for OSCAR data and Eq. (A2) adjusts the predicted position based on this change. Based on the empirically derived correction factor, it can be seen that the actual robot changes orientation by 15% of the idealized model prediction. The validated model response (gray dashed lines) is compared with the experimental data in Fig. 17. As can be seen, the validated model predicts OSCAR motion with a high level of accuracy across multiple locomotion cycles.

References

[1] Rus, D., and Tolley, M. T., 2015, "Design, Fabrication and Control of Soft Robots," Nature, **521**(7553), pp. 467–475.
[2] Kim, S., Laschi, C., and Trimmer, B., 2013, "Soft Robotics: A Bioinspired Evolution in Robotics," Trends Biotechnol., **31**(5), pp. 287–294.
[3] Tolley, M. T., Shepherd, R. F., Mosadegh, B., Galloway, K. C., Wehner, M., Karpelson, M., Wood, R. J., and Whitesides, G. M., 2014, "A Resilient, Untethered Soft Robot," Soft Rob., **1**(3), pp. 213–223.

[4] Hawkes, E. W., Blumenschein, L. H., Greer, J. D., and Okamura, A. M., 2017, "A Soft Robot That Navigates Its Environment Through Growth," Sci. Rob., **2**(8), pp. 1–8.

[5] Greer, J. D., Blumenschein, L. H., Okamura, A. M., and Hawkes, E. W., 2018, "Obstacle-Aided Navigation of a Soft Growing Robot," 2018 IEEE International Conference on Robotics and Automation (ICRA), Brisbane, Australia, May 21–25, pp. 4165–4172.

[6] Lee, J. Y., Kang, B. B., Lee, D. Y., Baek, S. M., Kim, W. B., Choi, W. Y., Song, J. R., Joo, H. J., Park, D., and Cho, K. J., 2016, "Development of a Multi-Functional Soft Robot (SNUMAX) and Performance in RoboSoft Grand Challenge," Front. Rob. AI, **3**(63), pp. 1–11.

[7] Fang, H., Zhang, Y., and Wang, K. W., 2017, "Origami-Based Earthworm-Like Locomotion Robots," Bioinspiration & Biomimetics, **12**(6), p. 065003.

[8] Jayaram, K., and Full, R. J., 2016, "Cockroaches Traverse Crevices, Crawl Rapidly in Confined Spaces, and Inspire a Soft, Legged Robot," Proc. Natl Acad. Sci. USA, **113**(8), pp. E950–E957.

[9] Rus, D., and Tolley, M. T., 2018, "Design, Fabrication and Control of Origami Robots," Nat. Rev. Mater., **3**(6), pp. 101–112.

[10] Banerjee, H., Pusalkar, N., and Ren, H., 2018, "Single-Motor Controlled Tendon-Driven Peristaltic Soft Origami Robot," ASME J. Mech. Rob., **10**(6), p. 064501.

[11] Zhang, K., Qiu, C., and Dai, J. S., 2016, "An Extensible Continuum Robot With Integrated Origami Parallel Modules," ASME J. Mech. Rob., **8**(3), p. 031010.

[12] Laschi, C., Mazzolai, B., and Cianchetti, M., 2016, "Soft Robotics: Technologies and Systems Pushing the Boundaries of Robot Abilities," Sci. Rob., **1**(1), p. eaah3690.

[13] Dollar, A. M., Cho, K. -J., Fearing, R. S., and Park, Y. -L., 2015, "Special Issue: Fabrication of Fully Integrated Robotic Mechanisms," ASME J. Mech. Rob., **7**(2), p. 020201.

[14] Firouzeh, A., and Paik, J., 2015, "Robogami: A Fully Integrated Low-Profile Robotic Origami," ASME J. Mech. Rob., **7**(2), p. 021009.

[15] Zhakypov, Z., Mori, K., Hosoda, K., and Paik, J., 2019, "Designing Minimal and Scalable Insect-Inspired Multi-locomotion Millirobots," Nature, **571**(7765), pp. 381–386.

[16] Onal, C. D., Wood, R. J., and Rus, D., 2013, "An Origami-Inspired Approach to Worm Robots," IEEE/ASME Trans. Mechatron., **18**(2), pp. 430–438.

[17] Wheeler, C. M., and Culpepper, M. L., 2016, "Soft Origami: Classification, Constraint, and Actuation of Highly Compliant Origami Structures," ASME J. Mech. Rob., **8**(5), p. 051012.

[18] Pierre, R. S., and Bergbreiter, S., 2019, "Toward Autonomy in Sub-Gram Terrestrial Robots," Annu. Rev. Control Rob. Auton. Syst., **2**(1), pp. 231–252.

[19] Goldberg, B., Zufferey, R., Doshi, N., Helbling, E. F., Whittredge, G., Kovac, M., and Wood, R. J., 2018, "Power and Control Autonomy for High-Speed Locomotion with an Insect-Scale Legged Robot," IEEE Rob. Autom. Lett., **3**(2), pp. 987–993.

[20] Angatkina, O., Chien, B., Pagano, A., Yan, T., Alleyne, A., Tawfick, S., and Wissa, A., 2017, "A Metameric Crawling Robot Enabled by Origami and Smart Materials," ASME 2017 Smart Materials, Adaptive Structures and Intelligent Systems, Snowbird, UT, Sept. 18–20, Vol. 1, ASME, p. V001T06A008.

[21] Luo, M., Yan, R., Wan, Z., Qin, Y., Santoso, J., Skorina, E. H., and Onal, C. D., 2018, "OriSnake: Design, Fabrication, and Experimental Analysis of a 3-D Origami Snake Robot," IEEE Rob. Autom. Lett., **3**(3), pp. 1993–1999.

[22] Miyashita, S., Guitron, S., Ludersdorfer, M., Sung, C. R., and Rus, D., 2015, "An Untethered Miniature Origami Robot That Self-folds, Walks, Swims, and Degrades," 2015 IEEE International Conference on Robotics and Automation (ICRA), Seattle, WA, May 25–30, IEEE, pp. 1490â1496.

[23] Miyashita, S., Guitron, S., Yoshida, K., Li, S., Damian, D. D., and Rus, D., 2016, "Ingestible, Controllable, and Degradable Origami Robot for Patching Stomach Wounds," 2016 IEEE International Conference on Robotics and Automation, Stockholm, Sweden, May 16–20, IEEE, pp. 909–916.

[24] Rich, S. I., Wood, R. J., and Majidi, C., 2018, "Untethered Soft Robotics," Nat. Electron., **1**(2), pp. 102–112.

[25] Angatkina, O., Gustafson, K., Wissa, A., and Alleyne, A. G., 2019, "Path Following for the Origami Crawling Robot," ASME 2019 Dynamic Systems and Control Conference, Park City, UT, Oct. 8 –11, pp. 1–9.

[26] Pagano, A., Yan, T., Chien, B., Wissa, A., and Tawfick, S., 2017, "A Crawling Robot Driven by Multi-Stable Origami," Smart Mater. Struct., **26**(9), p. 094007.

[27] Gustafson, K., Angatkina, O., and Wissa, A., 2020, "Model-Based Design of a Multistable Origami-Enabled Crawling Robot," Smart Mater. Struct., **29**(1), p. 015013.

[28] Yim, M., Shen, W.-M., Salemi, B., Rus, D., Moll, M., Lipson, H., and Klavins, E., 2007, "Modular Self-reconfigurable Robot Systems [Grand Challenges of Robotics]," IEEE Rob. Autom. Mag., **14**(1), pp. 43–52.

[29] Sohal, S. S., Sebastian, B., and Ben-Tzvi, P., 2021, "Autonomous Docking of Hybrid-Wheeled Modular Robots With an Integrated Active Genderless Docking Mechanism," J. Mech. Rob., **14**(1), p. 011010.

[30] Seok, S., Onal, C. D., Cho, K.-J., Wood, R. J., Rus, D., and Kim, S., 2013, "Meshworm: A Peristaltic Soft Robot with Antagonistic Nickel Titanium Coil Actuators," IEEE/ASME Trans. Mechatron., **18**(5), pp. 1485–1497.

[31] Fang, H., Zhang, Y., Wang, K. W., and Park, G., 2017, "An Earthworm-Like Robot Using Origami-Ball Structures," Active and Passive Smart Structures and Integrated Systems 2017, Portland, OR, Mar. 26–29, Vol. 10164, SPIE, pp. 229–238.

[32] Dolgov, D., Thrun, S., Montemerlo, M., and Diebel, J., 2008, "Practical Search Techniques in Path Planning for Autonomous Driving Introduction and Related Work," Ann Arbor, **1001**(48105), pp. 18–80.

[33] Kurzer, K., 2016, *Path Planning in Unstructured Environments: A Real-time Hybrid A* Implementation for Fast and Deterministic Path Generation for the KTH Research Concept Vehicle*, Master's thesis, KTH Royal Institute of Technology, Stockholm, Sweden.

[34] Petereit, J., Emter, T., Frey, C., Kopfstedt, T., and Beutel, A., 2012, "Application of Hybrid A* to an Autonomous Mobile Robot for Path Planning in Unstructured Outdoor Environments," ROBOTIK 2012; 7th German Conference on Robotics, Munich, Germany, May 21–22.

[35] Luo, M., 2017, *Pressure-Operated Soft Robotic Snake Modeling, Control, and Motion Planning*, Ph.D. thesis, Worcester Polytechnic Institute, Worcester, MA.

[36] Rajamani, R., 2012, *Vehicle Dynamics and Control*, 2nd ed., Springer Science & Business Media, New York.

[37] Fang, H., Li, S., Wang, K. W., and Xu, J., 2015, "Phase Coordination and Phase–Velocity Relationship in Metameric Robot Locomotion," Bioinspiration Biomimetics, **10**(6), p. 066006.

[38] Angatkina, O., 2021, *Design and Control of an Origami-Enabled Soft Crawling Autonomous Robot (OSCAR)*, Ph.D. thesis, University of Illinois Urbana-Champaign, Urbana, IL.